Journal of
Materials Chemistry A

ROYAL SOCIETY
OF CHEMISTRY

PAPER

View Article Online
View Journal | View Issue

Cite this: *J. Mater. Chem. A*, 2015, **3**, 23955

Efficient hole transport layers with widely tunable work function for deep HOMO level organic solar cells†

Jiaqi Cheng,‡[a] Fengxian Xie,‡[a] Yongsheng Liu,[b] Wei E. I. Sha,[a] Xinchen Li,[a]
Yang Yang*[b] and Wallace C. H. Choy*[a]

Received 31st August 2015
Accepted 26th October 2015

DOI: 10.1039/c5ta06878a

www.rsc.org/MaterialsA

Hole transport layers (HTLs) with large work function (WF) tuning ability for good energy level alignment with deep highest occupied molecular orbital (HOMO) level donor materials are desirable for high-performance and high open-circuit voltage (V_{OC}) organic solar cells (OSCs). Here, a novel low-temperature and solution-process approach to achieve WF tuning in HTLs is proposed. Specifically, the HTLs made from 2,3,4,5,6-pentafluorobenzylphosphonic acid (F5BnPA) incorporated graphene oxide (GO) and molybdenum oxide (MoO_x) solution (representing two possible classes of HTLs where carriers transport *via* valence and conduction bands, respectively) offer continuous WF tuning (the tuning range as large as 0.81 eV) by controlling F5BnPA's concentration. By employing a deep HOMO donor material, OSCs using the composite HTLs can achieve improved performances with largely increased V_{OC} (0.92 V for GO:F5BnPA *versus* 0.65 V for pristine GO; 0.91 V for MoO_x:F5BnPA *versus* 0.88 V for pristine MoO_x). The enhanced performance can be experimentally and theoretically explained by the decreased hole injection barrier (HIB) for GO or equivalent HIB (*i.e.* electron extraction barrier) for MoO_x and enhanced surface recombination velocity, which contribute to eliminating S-shaped current–voltage characteristics. Consequently, the incorporation of F5BnPA can efficiently tune HTL WF for high V_{OC} OSCs and extend HTL applications in organic electronics.

Introduction

As an attractive low-cost alternative to traditional photovoltaic technologies, organic solar cells (OSCs) have been experiencing a remarkable leap in power conversion efficiency (PCE) approaching over 10% both in single junction OSCs and in tandem OSCs during the past decade.[1–6] These substantial research advances benefit enormously from the engineering of material synthesis (novel organic photoactive polymers/small molecules),[7–9] film morphology,[10] device structure (normal/inverted and tandem structures),[11,12] interfacial carrier-transport layers[13–15] and the understanding of device physics.[16,17] Among these aspects, the interface between electrodes and active layers plays an important role in determining the performance of OSCs. The mismatched Fermi level of electrodes with the corresponding Fermi levels for holes and electrons of organic active layers will result in the formation of extraction/injection barriers at the interface, impairing the electrical properties and thus the device performance of OSCs.[18,19] Charge carrier selective contacts that extract holes (electrons) only and block the injection of counter electrons (holes) from organic active layers will reduce the loss of photogenerated charge carriers and raise the open-circuit voltage (V_{OC}).[20–23] Therefore, the design of functional carrier-transport layers between electrodes and organic active layers is highly important and desirable for high-performance OSCs.

Regarding hole transport layers (HTLs), poly(3,4-ethylenedioxythiophene):poly(styrene-sulfonate) (PEDOT:PSS) is commonly used as the HTL in fabricating standard OSCs. However, its long-term acidity and hygroscopic nature will induce poor stability of OSCs and then severely degrade devices.[24] Alternatively, various oxides have been developed as substitutes of PEDOT:PSS for high performance and stable OSCs. These oxides can be classified into two types according to their carrier transport mechanisms. Molybdenum oxide (MoO_x),[25–27] vanadium oxide (V_2O_5),[25,28] tungsten oxide (WO_3),[25,29] *etc.* have very large ionization potential (IP), which precluded hole transport *via* the valence band (VB). The hole extraction can be processed *via* electron transport from the electrode through the oxide conduction band (CB) to the highest occupied molecular orbital (HOMO) of organic donors.[25] Differently, for another class of oxides including graphene oxide

---

[a] *Department of Electrical and Electronic Engineering, The University of Hong Kong, Pokfulam Road, Hong Kong SAR, China. E-mail: chchoy@eee.hku.hk*

[b] *Department of Materials Science and Engineering, University of California, Los Angeles, Los Angeles, CA 90095, USA. E-mail: yangy@ucla.edu*

† Electronic supplementary information (ESI) available. See DOI: 10.1039/c5ta06878a

‡ These authors contributed equally to this work.

(GO),[30–32] nickel oxide (NiO_x),[14,33,34] *etc.*, hole transport *via* the VB of the metal oxide is favorable. The WF of these HTL materials (PEDOT:PSS 5.1 eV, GO 4.9 eV, NiO_x 5.4 eV, MoO_x 5.3 eV, V_2O_5 5.4 eV, and WO_3 5.35 eV) can align well with the HOMO levels of many typical organic photoactive donors such as poly(3-hexylthiophene) (P3HT) (5.1 eV), and polythieno[3,4-*b*]-thiophene-*co*-benzodithiophene (PTB7) (5.14 eV).[35] Importantly, high V_{OC} values contribute to the realization of high-performance OSCs. Since the maximum value of the V_{OC} is determined by the energy offset between the HOMO level of the donor and the lowest occupied molecular orbital (LUMO) level of the acceptor, conjugated polymer/small molecule donor materials with deep HOMO levels (typically > 5.5 eV) are attractive for obtaining high V_{OC} values. To avoid the formation of a hole injection barrier (HIB) at the interface, designing suitable HTL materials for these polymer/small molecule donor materials with deep HOMO levels is highly desirable.

The design of ideal HTL materials for these deep HOMO-level polymers/small molecules, combining the requirements of a smooth surface, good tuning ability of indium-tin oxide (ITO) WF and good electron blocking ability with efficient hole transport, remains challenging. Several WF tuning methods of GO have been reported, including O_2 plasma treatment,[36] sulfuration,[37] chlorination,[32] photo chlorination[38] and pre-oxidization.[39] Besides, WF tuning methods of GO for electron transporting layer (ETL) application have also been reported, including cesium neutralization[40] and lithium-neutralization.[41] More details can be found from the review article by Liu *et al.*[42] However, all the reported WF tuning methods for HTL application need energy-wasting and complex chemical reaction processes. Moreover, the reported WF can only be modified to be as high as ~5.2 eV, which is still not high enough to match with deep HOMO level (>5.5 eV) donors. Solution-process phosphonic acid has been reported to be a good surface modifier of an oxide layer such as ITO,[43,44] zinc oxide (ZnO)[45–47] and NiO_x.[48] These modification effects are ascribed to the chemisorption between the phosphate group and the oxide layer surface, including covalent bonding, electrostatic interactions and hydrogen bonding.[49] While phosphonic acid modified ITO has been reported in OSCs using deep HOMO level donors, such as poly(*N*-9′-heptadecanyl-2,7-carbazole-*alt*-5,5-(4′,7′-di-2-thienyl-2′,1′,3′-benzothiadiazole)) (PCDTBT) and poly(*p*-phenylenevinylene) derivative (Super Yellow, SY), with improved V_{OC}, the surface modification process is accompanied by complicated procedures such as a long soaking process for 24 hours, complex rinse and dry procedures, as well as even high temperature annealing.[48,50–54] Consequently, it is of strong importance to develop a simple low-temperature and solution-process approach for designing effective HTL materials combining smooth surface, good ability of WF tuning and good electron blocking ability with efficient hole transport ability.

In this work, we demonstrate a facile low-temperature and solution-process method to design efficient phosphonic acid modified HTL materials (GO and MoO_x) with wide WF tuning capabilities for deep HOMO-level polymer/small molecule donors. By adding the controllable amount of 2,3,4,5,6-pentafluorobenzylphosphonic acid (F5BnPA) (as shown in ESI Fig. S1a†) in individual GO and MoO_x solutions, we can realize a tunable WF (the value can be as high as 5.78 eV) of resultant HTLs made from the two individual oxides on ITO substrates.† Employing a deep HOMO-level two-dimensional conjugated small molecule (SMPV1) donor, OSCs using the composite HTLs can achieve improved performance, especially with increased V_{OC} (0.65 V for pristine GO *versus* 0.92 V for GO:F5BnPA; 0.88 V for pristine MoO_x *versus* 0.91 V for MoO_x:F5BnPA). These performance improvements indicate the wide feasibility in the two classes of HTL materials (carrier transport *via* the CB and VB, respectively). The experimental and theoretical evidence shows that the enhanced performance in F5BnPA-modified OSCs can be explained by the decreased HIB and enhanced surface recombination velocity. This new approach can offer an effective means for tuning the WF of HTLs to be well aligned with deep HOMO-level polymer/small molecule donor materials, which provides a simple scheme to fabricate high V_{OC} and high-performance OSCs.

Results and discussion

Continuously and widely tuning the WF of HTL materials

For the current work, we incorporate different amounts of F5BnPA into GO and MoO_x solutions for forming HTL with continuous and controllable tuning of WF. Details of the oxide solution and films preparation have been described in the Experimental section. Solutions of GO:F5BnPA and MoO_x:F5BnPA with different concentrations of F5BnPA are prepared by simply adding different amounts of F5BnPA into GO and MoO_x solutions, respectively. Kelvin-Probe measurements are employed to investigate the WF variation through incorporating different concentrations of F5BnPA, as shown in Table 1. The pristine GO film on ITO substrates exhibits a WF of 4.91 eV, which does not match well with deep HOMO-level polymer/small molecule donor materials (typically >5.5 eV). After adding different concentrations of F5BnPA, the WF of the composite film can be tuned continuously from 4.91 eV to 5.72 eV (*i.e.* WF variation of 0.81 eV). Similarly, the WF of MoO_x:F5BnPA can be adjusted from 5.30 eV (pristine MoO_x) to 5.78 eV at the additive concentration of 1 mg mL^{-1}. The WF tuning variations for GO:F5BnPA and MoO_x:F5BnPA HTLs measured by using a Kelvin-Probe are 0.81 eV and 0.48 eV, respectively.

Table 1 The WF of GO and MoO_x films with different concentrations of F5BnPA characterized by Kelvin-Probe measurements. ΔE_F is defined as the energy level offsets of the composite film and pristine films. The WF of ITO is listed for comparison

Concentrations of F5BnPA (mg mL^{-1})	GO:F5BnPA		MoO_x:F5BnPA	
	W_F (eV)	ΔE_F (eV)	W_F (eV)	ΔE_F (eV)
ITO	4.69			
w/o	4.91	0	5.30	0
0.1	5.13	0.22	5.48	0.18
0.25	5.43	0.52	5.52	0.22
0.5	5.52	0.61	5.58	0.28
0.75	5.65	0.74	5.67	0.37
1	5.72	0.81	5.78	0.48

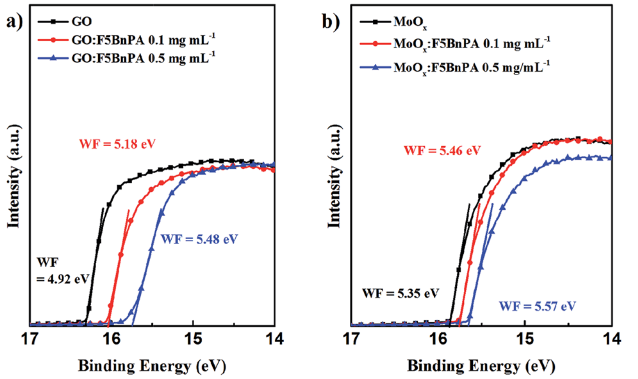

Fig. 1 (a) UPS spectra of the pristine GO film and GO:F5BnPA composite films. (b) UPS spectra of the pristine MoO_x film and MoO_x:F5BnPA composite films. The concentrations of F5BnPA are zero (pristine oxide), 0.1 mg mL^{-1} and 0.5 mg mL^{-1}.

To further clarify the capability of WF tuning by F5BnPA additive in oxide HTL materials, these films are characterized by ultraviolet photoelectron spectra (UPS) and Kelvin-Probe force microscope (KPFM), as shown in Fig. 1 and S2.† It can be seen from Fig. 1a that the pristine GO films show a WF of 4.92 eV that is consistent with other reports.[30] After adding two different amounts of F5BnPA, 0.1 mg mL^{-1} and 0.5 mg mL^{-1}, the corresponding resultant films show increased WF of 5.18 eV and 5.48 eV, respectively. Similarly, Fig. 1b shows that the results of MoO_x film in which WF is 5.35 eV (pristine MoO_x), 5.46 eV (0.1 mg mL^{-1} of F5BnPA) and 5.57 eV (0.5 mg mL^{-1} of F5BnPA). Evidently, the UPS spectra further confirm this continuously tuning the WF of F5BnPA-modified GO and MoO_x composite films, which is consistent with the results obtained by Kelvin-Probe measurements. Fig. S2† shows the KPFM images of GO, GO:F5BnPA, MoO_x and MoO_x:F5BnPA. The concentration of F5BnPA is 0.1 mg mL^{-1}. The smooth surface potential reveals that good film quality is formed after the F5BnPA incorporation. And the more negative surface potential values after incorporation certify the WF increase as demonstrated by Kelvin-Probe characterization and UPS.[55]

This WF tuning might be ascribed to the chemisorption between F5BnPA and the oxide surface. As we all know, GO is a graphene sheet functionalized with epoxy and hydroxyl groups on its sheet panel and at the edges.[36] Heterocondensation and covalent bond formation will happen between phosphonate groups and hydroxyl groups.[49] Due to the presence of highly electronegative fluorine atoms on the aromatic ring of F5BnPA, a surface dipole pointing away from the surface forms on the surface, which results in the increase of WF as shown in ESI Fig. S3.† MoO_x is a layered crystal structure held by van der Waals forces with hydroxyl groups on the surface.[28,56] F5BnPA is also easily bound to metal oxide surfaces, which also results in a surface dipole and WF increase. Besides, the Lewis acidic property of MoO_x helps with the chemisorption.[57] Moreover, it is indicated that the WF change of GO is approximately twice the one for MoO_x. This phenomenon could be ascribed to the different thicknesses of GO and MoO_x. As the optimized thickness of GO and MoO_x for OSC applications is 2 nm and 8 nm respectively (see the following section) and only the surface dipole contributes to the WF change, GO shows larger WF change after blending with the same amount of F5BnPA. The broad tuning WF of F5BnPA-modified GO and MoO_x films enables the HTLs to match with deep HOMO-level donors in OSCs, such as 1,1-bis-(4-bis(4-methyl-phenyl)-amino-phenyl)-cyclohexane (TAPC, 5.5 eV),[58] PCDTBT, 5.5 eV, and [59] poly[*N*-9′-

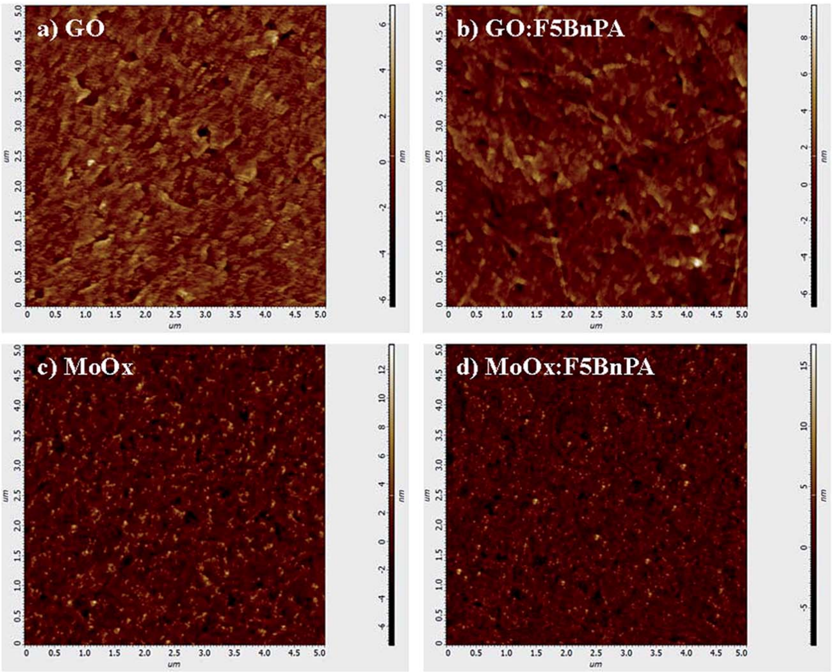

Fig. 2 AFM results of GO, GO:F5BnPA, MoO_x and MoO_x:F5BnPA films on ITO/glass substrates with the measured area of 5 × 5 μm.

heptadecanyl-2,7-carbazole-*alt*-5,5-(4,7-di-2-thienyl-5,6-bis(dodecyloxy)-2,1,3-benzothia-diazole)] PCDTBT12, 5.6 eV),[60] and to be used in other organic devices such as organic light emitting diodes.

The morphologies of GO, GO:F5BnPA, MoO_x and MoO_x:F5BnPA films have also been investigated by using a atomic force microscope (AFM) as shown in Fig. 2. The concentration of F5BnPA is 0.5 mg mL^{-1} for both GO and MoO_x. The root-mean-square (RMS) roughnesses of GO, GO:F5BnPA, MoO_x and MoO_x:F5BnPA are measured to be 1.11 nm, 1.37 nm, 1.93 nm and 2.22 nm, respectively. The small RMS indicates that GO and MoO_x can form a compact and smooth buffer layer on ITO substrates and the addition of F5BnPA has little influence on the roughness.

Performance of organic solar cells

To study the impact of F5BnPA-incorporated GO and MoO_x HTL films on device performance, a two-dimensional conjugated small molecule (SMPV1) with a deep HOMO level (5.51 eV)[1] is used as the donor material. [6,6]-phenyl C_{71}-butyric acid methyl ester ($PC_{71}BM$) is employed as the acceptor material. Their corresponding chemical structures are shown in ESI Fig. S1b.† OSCs with the structure of ITO/HTLs/SMPV1:$PC_{71}BM$/Ca/Al are fabricated, as detailed in the Experimental Section. The optimized film thickness of GO and MoO_x is 2 nm and 8 nm respectively as measured by using an ellipsometer. The device performance of OSCs with different thicknesses of GO and MoO_x is shown in ESI Fig. S4.†

The typical current density–voltage (*J*–*V*) curves under an AM 1.5 G illumination are shown in Fig. 3 and the performance of optimized OSCs is summarized in Table 2. By incorporating F5BnPA to form the GO:F5BnPA HTL (the concentration of F5BnPA is 0.5 mg mL^{-1}), the optimized OSCs achieve an increased short-circuit current density (J_{SC}) of 11.96 mA cm^{-2} (11.03 mA cm^{-2} for pristine GO OSC), largely increased V_{OC} of 0.92 V (0.65 V), fill factor (FF) of 46.59% (43.28%), and PCE of 5.13% (3.10%). Similarly, by replacing the MoO_x HTL with the MoO_x:F5BnPA HTL (the concentration of F5BnPA is 0.5 mg mL^{-1}), optimized devices display a gradually enhanced J_{SC} of

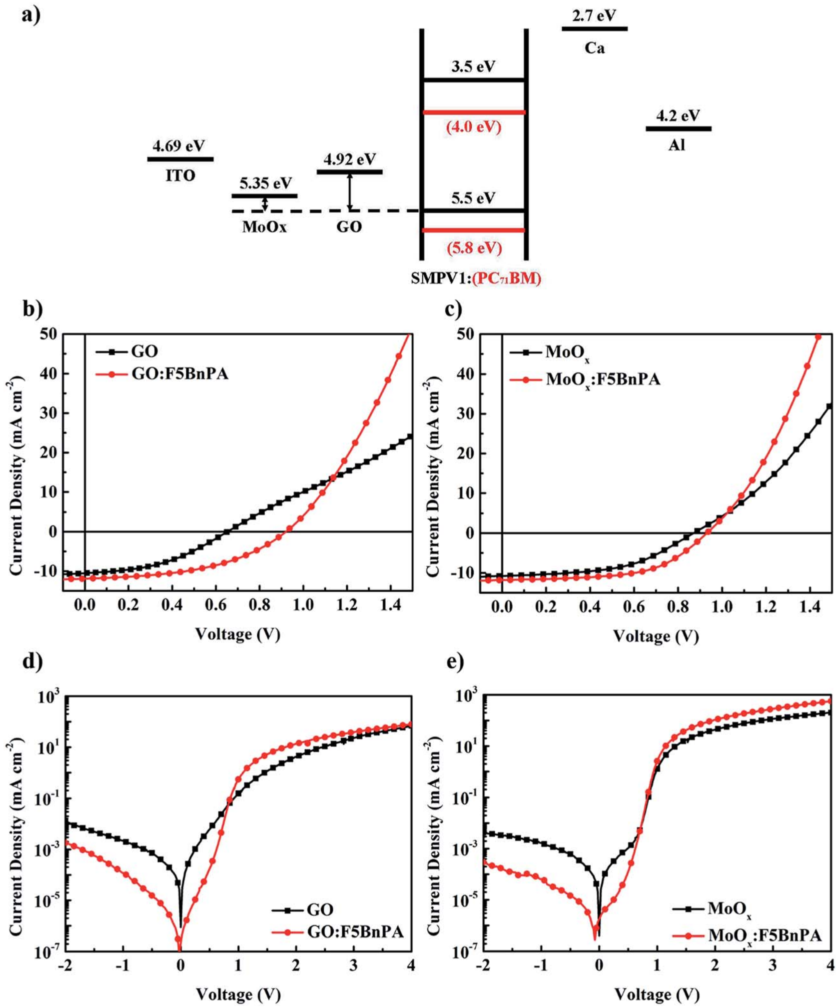

Fig. 3 (a) The schematic energy level diagram of OSCs. (b and c) Current density–voltage (*J*–*V*) characteristics of OSCs using different HTLs (the concentrations of F5BnPA are both 0.5 mg mL^{-1}) under illumination of simulated 100 mW cm^{-2} AM 1.5 G irradiation. (d and e) Corresponding dark *J*–*V* curves measured.

Table 2 Device performance of OSCs with the structure of ITO/HTL/SMPV1:$PC_{71}BM$/Ca/Al

	J_{SC} (mA cm^{-2})	V_{OC} (V)	FF (%)	PCE (%)
GO	11.03 ± 0.27	0.65 ± 0.01	43.28 ± 0.76	3.10 ± 0.14
GO:F5BnPA	11.96 ± 0.11	0.92 ± 0.01	46.59 ± 1.00	5.13 ± 0.18
MoO_x	10.96 ± 0.20	0.88 ± 0.01	50.81 ± 0.30	4.92 ± 0.10
MoO_x:F5BnPA	11.69 ± 0.27	0.91 ± 0.01	55.92 ± 0.90	5.96 ± 0.19

11.69 mA cm^{-2} (10.96 mA cm^{-2} for pristine MoO_x OSCs), a moderately enhanced V_{OC} of 0.91 V (0.88 V), a FF of 55.92% (50.81%), and a PCE of 5.96% (4.92%), which are comparable with those of PEDOT:PSS based devices as shown in Fig. S5 and Table S1.† The external quantum efficiency (EQE) spectra of these OSCs are illustrated in ESI Fig. S6.† Compared with OSCs using pristine GO or MoO_x HTLs, OSCs using the F5BnPA incorporated HTLs achieve higher EQE. Moreover, S-shaped deformation of *J*–*V* characteristics is also observed in OSCs using pristine GO or MoO_x HTLs (Fig. 3b and c). After incorporating F5BnPA, these S-shaped *J*–*V* characteristics are eliminated. The underlying physics will be discussed below in detail experimentally and theoretically.

The performance improvement and the elimination of S-shape *J*–*V* curve can be analyzed through the schematic energy level diagram as shown in Fig. 3a. When a pristine GO film is used as the HTL, there is a large energy level offset (*ca.* 0.6 eV) at the ITO/active layer interface. The energy level offset is *ca.* 0.15 eV when pristine MoO_x is used at the HTL. Typically, the V_{OC} is determined by the built-in potential in OSCs.[61] For the unoptimized interface contact, the WF of electrodes will limit the V_{OC}. Thus, the larger energy level offset in GO based devices results in the bigger V_{OC} suppression (0.27 V) compared with 0.03 V in MoO_x based devices. Furthermore, the large energy level offset can lead to the formation of hole injection barriers for GO (or equivalent hole injection barrier, *i.e.* electron extraction barrier for MoO_x), which has been reported to be responsible for the S-shaped *J*–*V* characteristics.[23,62] By introducing F5BnPA, the WF of HTLs is in good alignment with the HOMO level of donors, thus the interfacial energy loss will be minimized and V_{OC} can be increased. The decreased (equivalent) HIB also contributes to the suppression of S-shaped *J*–*V* curves. In addition, a dark current rectification ratio of approximately 300 for pristine GO based OCS at ±2 V is achieved as shown in Fig. 3d, which greatly increases to *ca.* 7500 for GO:F5BnPA based OSCs. For the MoO_x case, the rectification ratio increases from 1.0×10^5 (pristine MoO_x) to 3.5×10^5 for MoO_x:F5BnPA based OSCs, as shown in Fig. 3e. The largely increased rectification ratio for both cases indicates that GO/MoO_x:F5BnPA HTLs offer better alignment between ITO substrates and HOMO-level of donors, and thus provide a better hole injection contact.

To further illustrate the improvement of hole transporting properties, hole only devices with the structure of ITO/HTL/SMPV1:$PC_{71}BM$/MoO_x/Ag were fabricated. A comparison of the *J*–*V* characteristics is shown in Fig. S7.† The hole transportation gets enhanced after the incorporation of F5BnPA. Hole motilities were derived by fitting the *J*–*V* curves in the square law region according to the space charge limit current (SCLC) model and the Mott–Gurney law,[63]

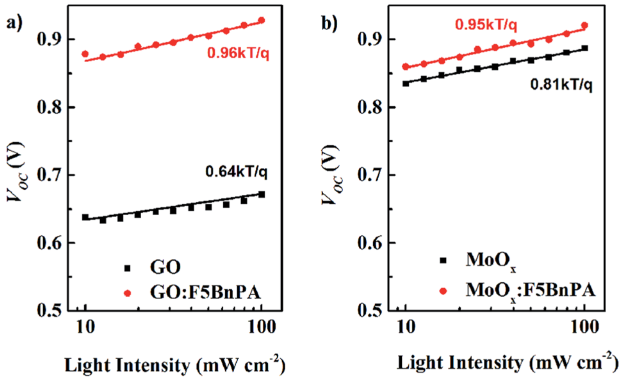

Fig. 4 Light intensity dependent V_{OC} in OSCs with different HTLs.

$$J = (9/8)\varepsilon_r\varepsilon_0\mu(V^2/L^3)$$

where *J* is the current density, ε_r is the relative permittivity, ε_0 is the permittivity of free space, μ is the hole mobility, *V* is the applied voltage, and *L* is the thickness of the active layer. Hole motilities of 3.04×10^{-5}, 6.76×10^{-5}, 5.77×10^{-5} and 1.07×10^{-4} $cm^2 V^{-1} s^{-1}$ have been determined for the devices with GO, GO:F5BnPA, MoO_x, and MoO_x:F5BnPA as HTLs. The improved hole mobility after the incorporation of F5BnPA indicates better hole transport in OSCs.

Fig. 4 shows the light intensity dependent V_{OC} for OSCs with and without the addition of F5BnPA. We can see a linear increase of V_{OC} by the logarithm scale of light intensity. The slopes of the devices based on GO and MoO_x HTLs are 0.64 and 0.81, which increase to 0.96 and 0.95 after separately introducing F5BnPA additives, indicating bimolecular recombination dominated recombination dynamics[64–66] in GO:F5BnPA and MoO_x:F5BnPA based OSCs. The changes of the slopes through the incorporation of different concentrations of F5BnPA observed as shown in Fig. 4 strongly depend on the (equivalent) hole injection barriers and surface recombination velocity as discussed in detail theoretically in the following section. The experimental and theoretical (as will be discussed later) studies show that the incorporation of F5BnPA in HTLs can reduce the HIB and enhance the surface recombination velocity.

Theoretical investigation on F5BnPA induced performance improvement

The electrical contact, which controls collection of photo-generated carriers (electrons and holes), is highly important to electrical properties of OSCs. An ideal contact should satisfy two essential requirements: (1) a zero injection barrier; (2) an infinite surface recombination velocity. A large injection barrier or finite surface recombination velocity will block and accumulate charges at electrodes and thus modify the built-in electrostatic field, which significantly degrades the electrical performance of OSCs. Meanwhile, to the best of our knowledge, few theoretical studies systemically investigated the evolution of the relationship between V_{OC} and incident light intensity (I) as the electrode interface is modified. This investigation is highly important to electrode-related device physics and thus to high-efficient solar cells.

To investigate the influence of different anode configurations (GO, MoO_x, GO:F5BnPA and MoO_x:F5BnPA) on the electrical properties of OSCs, semiconductor equations (Poisson, drift-diffusion, and continuity equations) are solved self-consistently (see the Theoretical Model in the Experimental section). The cathode can be regarded as a good ohmic contact by using the Ca/Al electrode. Fig. 5 shows the simulated J–V characteristics of OSCs with different injection barriers at the anode-active layer interface. When the (equivalent) injection barrier is formed at the interface, the J–V curve at the forward bias regime will bend toward high-voltage direction and meanwhile V_{OC} is reduced. These features agree well with the experimental results of Fig. 3b and c. The experimental J–V characteristics of pristine GO and MoO_x cases show noticeable curve bending in the forward bias regime, compared to the cases with GO:F5BnPA and MoO_x:F5BnPA. The large mismatch between HOMO of SMPV1 and GO WF induces a large HIB at the anode and thus a low V_{OC}. After introducing the F5BnPA into the GO, the reduced barrier contributes to the largely improved V_{OC} and S-shaped J–V curve elimination.

The relationship between V_{OC} and I under different injection barrier and surface recombination velocity conditions at the anode is also studied. When an infinite surface recombination velocity of holes (majority carriers at the anode) is assumed (and unchanged), the slope of the curve ($V_{OC} \sim \log(I)$) is independent of the values of injection barriers, as shown in Fig. 6, which cannot explain the phenomenon observed in Fig. 4. However, when the surface recombination velocity decreases (with the same injection barrier settings), we clearly see a reduced slope depicted in Fig. 7. This interesting finding is well coincident with the experimental results illustrated in Fig. 4. From the above theoretical analysis and the experimental results in the previous section, the introduction of F5BnPA not only reduces the (equivalent) injection barrier but also increases the surface recombination velocity between GO or the MoO_x anode and active layers. As a consequence, hole collection is remarkably improved by the incorporation of F5BnPA in HTLs. The eliminated S-shaped J–V characteristics (Fig. 3b), enhanced V_{OC} (Fig. 3b and c), and increased slope of $V_{OC} \sim \log(I)$ curve (Fig. 4) are experimentally and theoretically verified and explained by the improved electrical properties of OSCs by the incorporation of F5BnPA in HTLs.

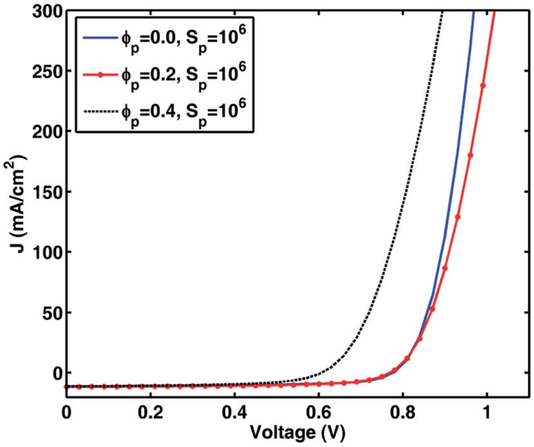

Fig. 5 Simulated J–V characteristics of OSCs with different injection barriers between the anode and active layer. An approximately infinite surface recombination velocity for holes at the anode (with a value of $S_p = 10^6$ m s^{-1}) is assumed. ϕ_p is the injection barrier at the anode with the unit of eV.

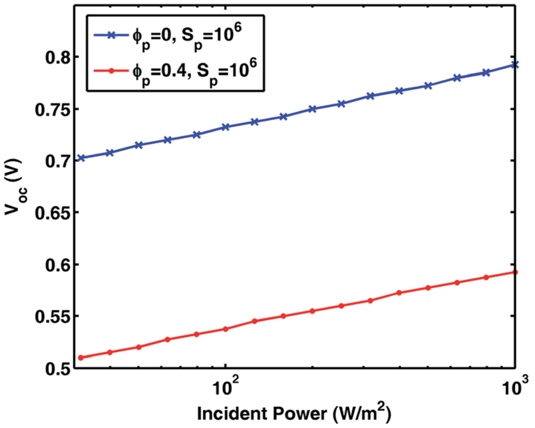

Fig. 6 Simulated V_{OC} *versus* incident light intensity with different injection barriers between the anode and active layer. An approximately infinite surface recombination velocity for holes at the anode (with a value of $S_p = 10^6$ m s^{-1}) is assumed.

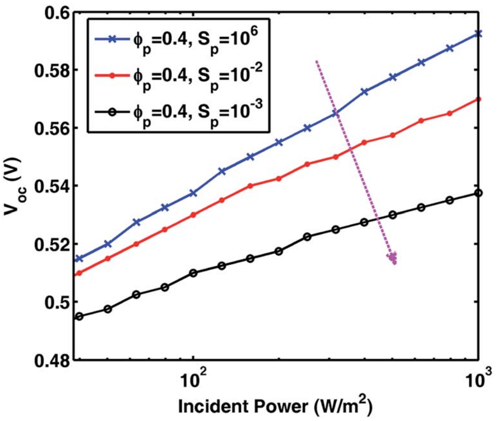

Fig. 7 Simulated open-circuit voltage V_{OC} *versus* incident light intensity with different surface recombination velocities S_p (unit: m s^{-1}) for holes at the anode. The same injection barrier of 0.4 eV between the anode and active layer is assumed.

Experimental section

Preparation of GO:F5BnPA and MoO_x:F5BnPA blend films

Molybdenum powder was purchased from Aladdin Industrial Inc. F5BnPA was purchased from Sigma-Aldrich. PEDOT:PSS

(Baytron Al 4083) was purchased from H. C. Starck GmbHm, Germany. Graphene oxide was synthesized by a reported modified Hummer's method[67] and was dispersed into ethanol under ultrasonication to form a 0.2 mg mL^{-1} solution. Molybdenum bronze solution was prepared by a former reported method.[26,28] Different amounts of F5BnPA were added into the two solutions to form blend solutions with certain concentrations, respectively. Different hole transport layers were prepared by spin-coating the mixed solutions onto clean ITO substrates at 4000 rpm for 40 s.

Devices fabrication

ITO glasses were cleaned by a standard procedure with detergent, acetone, and ethanol ultrasonic bath for each of 10 min, followed by an ultraviolet-ozone (UVO) treatment of 15 min. PEDOT:PSS was spin-coated on the treated ITO at 4000 rpm for 40 s and followed by 120 °C annealing for 20 min. The active layer was deposited by spin-coating the blend solution of SMPV1:PC$_{71}$BM at a weight ratio of 1 : 0.8 onto ITO/HTL substrates in a glove box at 2000 rpm. The blend solution was prepared in a solvent of chloroform. For the OSCs, calcium (20 nm) and aluminum (100 nm) were thermally evaporated onto the active layer through the same shadow mask under a pressure of 10^{-6} Torr. For the hole only devices, MoO$_x$ (10 nm) and silver (100 nm) were thermally evaporated.

Measurement and characterization

The *J–V* characterization of the OSCs was carried out under a light intensity of 100 mW cm^{-2} or dark by using a Keithley 2635 source meter with a step length of 0.01 V. The light was produced by using an ABET AM 1.5 G solar simulator and its intensity was calibrated by using a monocrystalline silicon standard solar cell. The more accurate V_{OC} values under different light intensities were obtained by *J–V* characterization around the open circuit state with a step length of 0.001 V. The WF of different hole transporting layers were measured by using an SKP 5050 Scanning Kelvin-Probe System (KP Technology Ltd.) with a resolution of 1–3 meV. The UPS was conducted using a He I discharged lamp (21.22 eV, Kratos Analytical). Height images and surface potential images were measured by using a tapping-mode AFM (NT-MDT, Moscow, Russia). The thicknesses of different HTLs were characterized by using a spectroscopic ellipsometer (J.A. WOOLLAM CO. INC.).

Theoretical model

The electrical properties of OSCs can be modeled by solving organic semiconductor equations involving Poisson, drift-diffusion and continuity equations[68,69]

$$\nabla\cdot(\varepsilon\nabla\phi) = -q(p-n) \tag{1}$$

$$\frac{\partial n}{\partial t} = \frac{1}{q}\nabla\cdot(-q\mu_n n\nabla\phi + qD_n\nabla n) + QG - (1-Q)R \tag{2}$$

$$\frac{\partial p}{\partial t} = -\frac{1}{q}\nabla\cdot(-q\mu_p p\nabla\phi - qD_p\nabla p) + QG - (1-Q)R \tag{3}$$

where q is the electron charge, ϕ is the potential, and n and p are electron and hole densities, respectively. Moreover, μ_n and μ_p are the mobility of electrons and holes, respectively. Furthermore, $D_n = \mu_n(k_BT/q)$ and $D_p = \mu_p(k_BT/q)$ are the diffusion coefficients of electrons and holes, respectively, where k_B and T are the Boltzmann constant and Kelvin temperature. $J_n = -q\mu_n n\nabla\phi + qD_n\nabla n$ and $J_p = -q\mu_p p\nabla\phi - qD_p\nabla p$ are, respectively, electron and hole current densities, and G is the exciton generation rate. Here, the recombination rate R is taken as the Langevin bimolecular form;[70] and the field-dependent exciton dissociation probability Q is evaluated by the Onsager–Braun theory.[71,72]

The potential boundary condition at the electrodes is given by

$$\phi = V - \frac{W_m}{q} \tag{4}$$

where V is the applied bias voltage and W_m is the WF of the electrode. For understanding the influence of electrodes on the electrical properties of OSCs, the current density (boundary conditions) at the Schottky contacts is given by

$$\text{Anode}\begin{cases} J_n^a = qS_n^a\left(n - n_{eq}^a\right) \\ J_p^a = qS_p^a\left(p - p_{eq}^a\right)\end{cases} \quad \text{cathode}\begin{cases} J_n^c = qS_n^c\left(n - n_{eq}^c\right) \\ J_p^c = qS_p^c\left(p - p_{eq}^c\right)\end{cases} \tag{5}$$

where S_n^a and S_p^a are the surface recombination velocity for electrons and holes at the anode; S_n^c and S_p^c are the surface recombination velocity for electrons and holes at the cathode. n_{eq} and p_{eq} are electron and hole densities with assumptions of surface infinite recombination velocities

$$\text{Anode}\begin{cases} n_{eq}^a = N_c \exp\left(\dfrac{-E_g + q\phi_p}{k_BT}\right) \\ p_{eq}^a = N_v \exp\left(\dfrac{-q\phi_p}{k_BT}\right)\end{cases} \quad \text{cathode}\begin{cases} n_{eq}^c = N_c \exp\left(\dfrac{-q\phi_n}{k_BT}\right) \\ p_{eq}^c = N_v \exp\left(\dfrac{-E_g + q\phi_n}{k_BT}\right)\end{cases} \tag{6}$$

where N_c and N_v are the effective density of states for bulk heterojunction active materials. ϕ_n and ϕ_p are injection barriers for the cathode and anode, respectively. In our simulation, $S_n^c \to \infty$, $S_p^c \to \infty$, $S_n^a \to \infty$ and $\phi_n = 0$. We modify ϕ_p and S_p^a to clarify the roles of the injection barrier and surface recombination velocities of holes (majorities) at the anode in affecting the electrical performance of OSCs.

Conclusions

To sum up, we propose and demonstrate an effective low-temperature and solution-process approach to tune the WF of HTLs for good energy level alignment between electrodes and deep HOMO-level donor materials. Distinctively, this wide WF tuning approach works in two different types of HTL materials represented by GO and MoO_x, whose carriers transport is *via* the VB and CB, respectively. Both Kelvin-Probe measurements and UPS results confirm that continuously tunable WF for GO and MoO_x HTLs is achieved after a simple F5BnPA incorporation. Employing a deep HOMO-level donor material of SMPV1, OSCs utilizing F5BnPA:GO and F5BnPA:GO MoO_x HTLs can achieve improved V_{OC} and J_{SC}, and thus greatly enhanced PCE compared with OSCs utilizing pristine GO and MoO_x HTLs. Our experimental and theoretical results show that the improved performance is attributed to the reduced (equivalent) injection barrier for enhancing the V_{OC} and increased surface recombination velocity for eliminating the S-shaped J–V. Therefore, our approach for introducing F5BnPA into HTLs could effectively improve the electrical properties of deep HOMO-level donor based OSCs. Consequently, the proposed new approach of F5BnPA incorporated GO and MoO_x HTLs with large WF tuning capacity makes an attractive contribution to the evolution of high V_{OC} OSCs with deep HOMO-level donors and can also be applied in other organic electronic devices.

Acknowledgements

J. C. and F. X. contributed equally to the work. This study was supported by the University Grant Council of the University of Hong Kong (Grants10401466 and 201111159062), the General Research Fund (Grants HKU711813), an RGC-NSFC Grant (N_HKU709/12), the Collaborative Research Fund (grant CUHK1/CRF/12 G) from the Research Grants Council of Hong Kong Special Administrative Region, China, and Grant CAS14601 from CAS-Croucher Funding Scheme for Joint Laboratories. We acknowledge the help and discussion of Hugh Zhu, Di Zhang and Shunmian Lu.

Notes and references

1 Y. Liu, C.-C. Chen, Z. Hong, J. Gao, Y. M. Yang, H. Zhou, L. Dou, G. Li and Y. Yang, *Sci. Rep.*, 2013, **3**, 3356.
2 J. You, L. Dou, K. Yoshimura, T. Kato, K. Ohya, T. Moriarty, K. Emery, C.-C. Chen, J. Gao, G. Li and Y. Yang, *Nat. Commun.*, 2013, **4**, 1446.
3 J.-D. Chen, C. Cui, Y.-Q. Li, L. Zhou, Q.-D. Ou, C. Li, Y. Li and J.-X. Tang, *Adv. Mater.*, 2015, **27**, 1035–1041.
4 X. Che, X. Xiao, J. D. Zimmerman, D. Fan and S. R. Forrest, *Adv. Energy Mater.*, 2014, **4**, 1400568.
5 Z. He, B. Xiao, F. Liu, H. Wu, Y. Yang, S. Xiao, C. Wang, T. P. Russell and Y. Cao, *Nat. Photonics*, 2015, **9**, 174–179.
6 Y. Liu, J. Zhao, Z. Li, C. Mu, W. Ma, H. Hu, K. Jiang, H. Lin, H. Ade and H. Yan, *Nat. Commun.*, 2014, **5**, 5293.
7 B. Kan, Q. Zhang, M. Li, X. Wan, W. Ni, G. Long, Y. Wang, X. Yang, H. Feng and Y. Chen, *J. Am. Chem. Soc.*, 2014, **136**, 15529–15532.
8 G. Yu, J. Gao, J. C. Hummelen, F. Wudl and A. J. Heeger, *Science*, 1995, **270**, 1789–1790.
9 M. C. Scharber, M. Koppe, J. Gao, F. Cordella, M. A. Loi, P. Denk, M. Morana, H.-J. Egelhaaf, K. Forberich, G. Dennler, R. Gaudiana, D. Waller, Z. Zhu, X. Shi and C. J. Brabec, *Adv. Mater.*, 2010, **22**, 367–370.
10 G. Li, V. Shrotriya, J. Huang, Y. Yao, T. Moriarty, K. Emery and Y. Yang, *Nat. Mater.*, 2005, **4**, 864–868.
11 S. Lu, X. Guan, X. Li, W. E. I. Sha, F. Xie, H. Liu, J. Wang, F. Huang and W. C. H. Choy, *Adv. Energy Mater.*, 2015, **5**, 1500631.
12 H. Zhou, Y. Zhang, C.-K. Mai, S. D. Collins, G. C. Bazan, T.-Q. Nguyen and A. J. Heeger, *Adv. Mater.*, 2015, **27**, 1767–1773.
13 T. Yang, M. Wang, C. Duan, X. Hu, L. Huang, J. Peng, F. Huang and X. Gong, *Energy Environ. Sci.*, 2012, **5**, 8208–8214.
14 F. Jiang, W. C. H. Choy, X. Li, D. Zhang and J. Cheng, *Adv. Mater.*, 2015, **27**, 2930–2937.
15 A. Varotto, N. D. Treat, J. Jo, C. G. Shuttle, N. A. Batara, F. G. Brunetti, J. H. Seo, M. L. Chabinyc, C. J. Hawker, A. J. Heeger and F. Wudl, *Angew. Chem., Int. Ed.*, 2011, **50**, 5166–5169.
16 L. Dou, J. You, Z. Hong, Z. Xu, G. Li, R. A. Street and Y. Yang, *Adv. Mater.*, 2013, **25**, 6642–6671.
17 X. Gong, M. Tong, F. G. Brunetti, J. Seo, Y. Sun, D. Moses, F. Wudl and A. J. Heeger, *Adv. Mater.*, 2011, **23**, 2272–2277.
18 P. W. Blom, V. D. Mihailetchi, L. J. A. Koster and D. E. Markov, *Adv. Mater.*, 2007, **19**, 1551–1566.
19 W. Tress, K. Leo and M. Riede, *Adv. Funct. Mater.*, 2011, **21**, 2140–2149.
20 J. Reinhardt, M. Grein, C. Bühler, M. Schubert and U. Würfel, *Adv. Energy Mater.*, 2014, **4**, 1400081.
21 E. L. Ratcliff, A. Garcia, S. A. Paniagua, S. R. Cowan, A. J. Giordano, D. S. Ginley, S. R. Marder, J. J. Berry and D. C. Olson, *Adv. Energy Mater.*, 2013, **3**, 647–656.
22 C.-Z. Li, C.-Y. Chang, Y. Zang, H.-X. Ju, C.-C. Chueh, P.-W. Liang, N. Cho, D. S. Ginger and A. K. Y. Jen, *Adv. Mater.*, 2014, **26**, 6262–6267.
23 A. Wagenpfahl, D. Rauh, M. Binder, C. Deibel and V. Dyakonov, *Phys. Rev. B: Condens. Matter Mater. Phys.*, 2010, **82**, 115306.
24 M. Jørgensen, K. Norrman and F. C. Krebs, *Sol. Energy Mater. Sol. Cells*, 2008, **92**, 686–714.
25 J. Meyer, S. Hamwi, M. Kröger, W. Kowalsky, T. Riedl and A. Kahn, *Adv. Mater.*, 2012, **24**, 5408–5427.
26 X. Li, W. C. H. Choy, F. Xie, S. Zhang and J. Hou, *J. Mater. Chem. A*, 2013, **1**, 6614–6621.
27 V. Shrotriya, G. Li, Y. Yao, C.-W. Chu and Y. Yang, *Appl. Phys. Lett.*, 2006, **88**, 073508.
28 F. Xie, W. C. H. Choy, C. Wang, X. Li, S. Zhang and J. Hou, *Adv. Mater.*, 2013, **25**, 2051–2055.

29 S. Han, W. S. Shin, M. Seo, D. Gupta, S.-J. Moon and S. Yoo, *Org. Electron.*, 2009, **10**, 791–797.
30 S.-S. Li, K.-H. Tu, C.-C. Lin, C.-W. Chen and M. Chhowalla, *ACS Nano*, 2010, **4**, 3169–3174.
31 Y. Gao, H.-L. Yip, S. K. Hau, K. M. O'Malley, N. C. Cho, H. Chen and A. K.-Y. Jen, *Appl. Phys. Lett.*, 2010, **97**, 203306.
32 D. Yang, L. Zhou, W. Yu, J. Zhang and C. Li, *Adv. Energy Mater.*, 2014, **4**, 1400591.
33 M. D. Irwin, D. B. Buchholz, A. W. Hains, R. P. H. Chang and T. J. Marks, *Proc. Natl. Acad. Sci. U. S. A.*, 2008, **105**, 2783–2787.
34 K. X. Steirer, J. P. Chesin, N. E. Widjonarko, J. J. Berry, A. Miedaner, D. S. Ginley and D. C. Olson, *Org. Electron.*, 2010, **11**, 1414–1418.
35 S. Chen, J. R. Manders, S.-W. Tsang and F. So, *J. Mater. Chem.*, 2012, **22**, 24202–24212.
36 D. Yang, L. Zhou, L. Chen, B. Zhao, J. Zhang and C. Li, *Chem. Commun.*, 2012, **48**, 8078–8080.
37 J. Liu, Y. Xue and L. Dai, *J. Phys. Chem. Lett.*, 2012, **3**, 1928–1933.
38 E. Stratakis, K. Savva, D. Konios, C. Petridis and E. Kymakis, *Nanoscale*, 2014, **6**, 6925–6931.
39 C. Li, X. Yang, Y. Zhao, P. Zhang, Y. Tu and Y. Li, *Org. Electron.*, 2014, **15**, 2868–2875.
40 J. Liu, Y. H. Xue, Y. X. Gao, D. S. Yu, M. Durstock and L. M. Dai, *Adv. Mater.*, 2012, **24**, 2228–2233.
41 G. Kakavelakis, D. Konios, E. Stratakis and E. Kymakis, *Chem. Mater.*, 2014, **26**, 5988–5993.
42 J. Liu, M. Durstock and L. Dai, *Energy Environ. Sci.*, 2014, **7**, 1297–1306.
43 A. Sharma, A. Haldi, W. J. Potscavage Jr, P. J. Hotchkiss, S. R. Marder and B. Kippelen, *J. Mater. Chem.*, 2009, **19**, 5298–5302.
44 P. J. Hotchkiss, H. Li, P. B. Paramonov, S. A. Paniagua, S. C. Jones, N. R. Armstrong, J.-L. Brédas and S. R. Marder, *Adv. Mater.*, 2009, **21**, 4496–4501.
45 N. Kedem, S. Blumstengel, F. Henneberger, H. Cohen, G. Hodes and D. Cahen, *Phys. Chem. Chem. Phys.*, 2014, **16**, 8310–8319.
46 I. Lange, S. Reiter, M. Pätzel, A. Zykov, A. Nefedov, J. Hildebrandt, S. Hecht, S. Kowarik, C. Wöll, G. Heimel and D. Neher, *Adv. Funct. Mater.*, 2014, **24**, 7014–7024.
47 I. Lange, S. Reiter, J. Kniepert, F. Piersimoni, M. Pätzel, J. Hildebrandt, T. Brenner, S. Hecht and D. Neher, *Appl. Phys. Lett.*, 2015, **106**, 113302.
48 A. Bulusu, S. A. Paniagua, B. A. MacLeod, A. K. Sigdel, J. J. Berry, D. C. Olson, S. R. Marder and S. Graham, *Langmuir*, 2013, **29**, 3935–3942.
49 P. J. Hotchkiss, S. C. Jones, S. A. Paniagua, A. Sharma, B. Kippelen, N. R. Armstrong and S. R. Marder, *Acc. Chem. Res.*, 2011, **45**, 337–346.
50 A. M. Bradley, E. H. Noah, L. R. Erin, L. J. Judith, R. A. Neal, J. G. Anthony, J. H. Peter, R. M. Seth, T. C. Charles and S. G. David, *J. Phys. Chem. Lett.*, 2012, **3**, 1202–1207.
51 K. M. Knesting, H. Ju, C. W. Schlenker, A. J. Giordano, A. Garcia, O. N. L. Smith, D. C. Olson, S. R. Marder and D. S. Ginger, *J. Phys. Chem. Lett.*, 2013, **4**, 4038–4044.
52 H. Wang, E. D. Gomez, Z. Guan, C. Jaye, M. F. Toney, D. A. Fischer, A. Kahn and Y.-L. Loo, *J. Phys. Chem. C*, 2013, **117**, 20474–20484.
53 G. Shao, M. S. Glaz, F. Ma, H. Ju and D. S. Ginger, *ACS Nano*, 2014, **8**, 10799–10807.
54 R. C. Sarah, V. L. Jian, C. O. Dana and L. R. Erin, *Adv. Energy Mater.*, 2014, **5**, 1400549.
55 D. J. Ellison, B. Lee, V. Podzorov and C. D. Frisbie, *Adv. Mater.*, 2011, **23**, 502–507.
56 A. van Hengstum, J. van Ommen, H. Bosch and P. Gellings, *Appl. Catal.*, 1983, **5**, 207–217.
57 A. M. Turek, I. E. Wachs and E. DeCanio, *J. Phys. Chem.*, 1992, **96**, 5000–5007.
58 M. Zhang, H. Wang, H. Tian, Y. Geng and C. W. Tang, *Adv. Mater.*, 2011, **23**, 4960–4964.
59 L. Huo, J. Hou, S. Zhang, H.-Y. Chen and Y. Yang, *Angew. Chem., Int. Ed.*, 2010, **49**, 1500–1503.
60 J. Sun, Y. Zhu, X. Xu, L. Lan, L. Zhang, P. Cai, J. Chen, J. Peng and Y. Cao, *J. Phys. Chem. C*, 2012, **116**, 14188–14198.
61 O. J. Sandberg, M. Nyman and R. Österbacka, *Phys. Rev. Appl.*, 2014, **1**, 024003.
62 D. Zhang, W. C. H. Choy, F. Xie, W. E. I. Sha, X. Li, B. Ding, K. Zhang, F. Huang and Y. Cao, *Adv. Funct. Mater.*, 2013, **23**, 4255–4261.
63 A. M. Goodman and A. Rose, *J. Appl. Phys.*, 1971, **42**, 2823–2830.
64 M. M. Mandoc, F. B. Kooistra, J. C. Hummelen, B. de Boer and P. W. M. Blom, *Appl. Phys. Lett.*, 2007, **91**, 263505.
65 V. D. Mihailetchi, H. Xie, B. de Boer, L. J. A. Koster and P. W. Blom, *Adv. Funct. Mater.*, 2006, **16**, 699–708.
66 L. J. A. Koster, V. D. Mihailetchi, R. Ramaker and P. W. M. Blom, *Appl. Phys. Lett.*, 2005, **86**, 123509.
67 M. Hirata, T. Gotou, S. Horiuchi, M. Fujiwara and M. Ohba, *Carbon*, 2004, **42**, 2929–2937.
68 S. Selberherr, *Analysis and simulation of semiconductor devices*, Springer, 1st edn, 1984.
69 L. J. A. Koster, E. C. P. Smits, V. D. Mihailetchi and P. W. M. Blom, *Phys. Rev. B: Condens. Matter Mater. Phys.*, 2005, **72**, 085205.
70 P. Langevin, *Ann. Chim. Phys.*, 1903, **28**, 122.
71 L. Onsager, *Phys. Rev.*, 1938, **54**, 554.
72 C. L. Braun, *J. Chem. Phys.*, 1984, **80**, 4157–4161.